RSC Advances

PAPER

View Article Online
View Journal | View Issue

Cite this: *RSC Adv.*, 2021, **11**, 10043

Achieving the potential multifunctional near-infrared materials $Ca_3In_{2-x}Ga_xGe_3O_{12}:Cr^{3+}$ using a solid state method†

Lingwei Cao, Panlai Li,* Jia Cui, Xuejiao Wang, Yao Yao, Mengya Zhang, Mingjie Zheng, Zhibin Yang, Hao Suo* and Zhijun Wang*

Near-infrared spectroscopy is developing rapidly in the fields of human detection and food analysis due to its fast response and non-invasive characteristics. Herein, we report the novel near-infrared garnet-type $Ca_3In_2Ge_3O_{12}:xCr^{3+}$ and $Ca_3In_{2-x}Ga_xGe_3O_{12}:0.07Cr^{3+}$ phosphors, in which there are two crystallographic sites (CaO_8, InO_6) that can be substituted by Cr^{3+}, and cation regulation engineering for In^{3+} is utilized to tune the luminescence properties. Under the 480 nm excitation, the $Ca_3In_2Ge_3O_{12}:xCr^{3+}$ phosphor emits a broad spectrum at 650–1150 nm, which matches well with the first biological window. The concentration quenching mechanism and luminescence mechanism of $Ca_3In_2Ge_3O_{12}:xCr^{3+}$ were studied and the site assignment of the two luminescence centers was discussed using low temperature spectra and fluorescence decay curves. The application performance of the phosphor was improved by introducing Ga^{3+} to substitute for In^{3+}, and the blue shift of nearly 50 nm was explained by crystal field and nephelauxetic effects. At the same time, a 24% increase in the activation energy of thermal quenching of phosphors was obtained, which has been analyzed using the mechanism of phonon transition and the change of structural rigidity. Thus, the near-infrared emitting $Ca_3In_{0.2}Ga_{1.8}Ge_3O_{12}:0.07Cr^{3+}$ phosphor was obtained, which has lower cost, higher emission intensity, and much better thermal stability, spreading the application of phosphors in plant far red light illumination, human body detection, and spectral conversion technology of silicon-based solar cells. Simultaneously, an example of a near-infrared plant illumination experiment is given, demonstrating that a cation substitution strategy based on crystal field control could be applied to tune spectral distribution and develop novel potential phosphors for practical optical application.

Received 26th January 2021
Accepted 1st March 2021

DOI: 10.1039/d1ra00682g

rsc.li/rsc-advances

1 Introduction

In recent years, near-infrared spectroscopy (NIR) technology has been developing rapidly. The luminescence of the first region (650–900 nm) and the second region (1000–1400 nm) has attracted much attention due to its low absorption in biological tissues.[1–3] For example, the absorption peak of deoxyhemoglobin in the human body is at 760 nm, and the absorption peak of oxyhemoglobin is at 900 nm, which opens the way for near-infrared light detection in blood.[4] The absorption region of plant phytochrome Pfr is 700–800 nm, and the absorption spectral range of photosynthetic bacterial chlorophyll is 715–1050 nm, which proves the potential of near-infrared light in the field of plant lighting.[5–7] Near-infrared light has different spectral responses to different substances in fruits. The content changes of water (970–980 nm) and soluble sugar (750–920 nm) can be characterized in the absorption spectra, which provides direction for the detection of fluorescent food powder.[8,9] Therefore, phosphors having these properties have been widely studied, such as $Mg_3Ga_2GeO_8:Cr^{3+}$,[10] $Ca_3Lu(Zr,Hf)_2Al_3O_{12}:Cr^{3+}$,[11] $Zn_3Ga_2Ge_2O_{10}:Cr^{3+}$,[12] $LaMgGa_{11}O_{19}:Cr^{3+}$,[13] *etc.* In addition, phosphor conversion light emitting diodes (pc-LEDs) have become high-quality radiation sources, near-infrared pc-LED researched in biological detection and night vision was fabricated by combining phosphor and the commercial blue light-emitting InGaN chip,[14,15] which puts forward new requirements for the thermal stability of phosphors. Therefore, it is of great significance to find a kind of phosphor which can be widely tuned in the near-infrared region and has relatively high thermal stability, which can be packaged into pc-LEDs with various potential applications.

Transition metal Cr^{3+} is an ideal activator for the preparation of near-infrared phosphors. The outer layer of Cr atom is easy to lose three electrons and form Cr^{3+}. The valence state of Cr^{3+} is stable and has high octahedral site selection energy.[16] Cr^{3+}

National-Local Joint Engineering Laboratory of New Energy Photoelectric Devices, Hebei Key Laboratory of Optic-electronic Information and Materials, College of Physics Science & Technology, Hebei University, Baoding 071002, China. E-mail: panlai@126.com; suo@hbu.edu.cn; wangzj1998@126.com

† Electronic supplementary information (ESI) available. See DOI: 10.1039/d1ra00682g

usually emits narrow-band light from the spin-forbidden transition ^2E–$^4A_2$ at 700 nm or a tunable broadband spectrum (600–1000 nm) from the spin-allowed transition $^4T_2$–$^4A_2$. At the same time, the luminescence performance can be greatly affected by the crystal field environment.[17,18] Garnet plays an important role in the reported Cr^{3+} doped matrix. In 2014, A. Zabiliūtė prepared Cr^{3+}-doped $Gd_3Ga_5O_{12}$, $Y_3Ga_5O_{12}$, $Lu_3Ga_5O_{12}$ and $Gd_3Sc_2Ga_3O_{12}$ far red garnet phosphors by sol–gel method, which are of great significance to greenhouse planting plant lighting.[19] Zhang reported that Cr^{3+}-doped $Ca_2LuZr_2Al_3O_{12}$ broadband near-infrared phosphor, and its internal quantum efficiency reached 69.1%.[20] Malysa studied the $X_3Sc_2Ga_3O_{12}$ (X = Lu, Y, Gd, La) material with a garnet structure. The FWHM of the spectra after doping Cr^{3+} is 172 nm, and the internal quantum efficiency can reach 60%.[21] The crystal structure of garnet is stable, and its general formula is $A_3B_2C_3O_{12}$. A represents eight coordinated divalent cations, B represents six coordinated trivalent cations, and C-site is a tetrahedral structure coordinated with four O^{2-},[22,23] so it can provide rich coordination for the implementation of flexible performance control means. Cr^{3+} often replaces the B site. Due to the matching of valence and coordination, phosphors doped with Cr^{3+} usually have good light-emitting performance. Currently one of the problems of commercial phosphors is poor thermal stability since the emission intensity of the phosphor will decrease when heat generates. The structural rigidity is a key factor that affects the thermal stability of the phosphor. Usually, solid state design is an effective way to solve this problem of phosphors. Due to rich composition of garnet-type phosphors, substitution of cation/anion or chemical unit could be used to change the luminescence properties.[24,25]

In this paper, a series of $Ca_3In_2Ge_3O_{12}$:xCr^{3+} phosphors were synthesized based on the luminescence characteristics of Cr^{3+} and the structural characteristics of garnet, and the concentration quenching and luminescence mechanism were studied in detail. Moreover, a solid state system $Ca_3In_{2-x}Ga_xGe_3O_{12}$:$xCr^{3+}$ was built to improve luminescence properties. As the result, the emission intensity has increased by five times, and its spectra were also more widely adapted with the first near-infrared region (650–900 nm). The shift of the spectra has been explained from the perspective of crystal field strength and the nephelauxetic effect. With the increase of structural rigidity, the thermal stability of the phosphor has increased by 24%, which improves its application potential in plant lighting, biological detection and solar energy spectra conversion technology.

2 Experimental

2.1 Sample preparation

Cr^{3+}-doped $Ca_3In_2Ge_3O_{12}$ (CIG) and $Ca_3In_{2-x}Ga_xGe_3O_{12}$ ($CI_{2-x}G_xG$) phosphors were synthesized by high temperature solid state method. $CaCO_3$ (99.99%), In_2O_3 (99.9%), Ga_2O_3 (99.9%), Ga_2O_3 (99.9%), Cr_2O_3 (99.99%) and GeO_2 (99.99%) were used as raw materials. The raw materials were mixed according to the chemical formula and weighed in an electronic scale with an error of less than 0.0001 g, and mixed and ground in an agate mortar for 30 minutes. Finally, the mixture is transferred to a corundum crucible and placed in a box furnace. At the heating rate of 5 °C min^{-1}, the temperature was raised to 500 °C for 1 hour, then to 1250 °C for 4 hours, and finally dropped to normal temperature at the rate of 5 °C min^{-1} and the procedure was ended. In this process, the samples were synthesized in air.

2.2 NIR pc-LED preparation

At first, mix the phosphor into the organic silica gel according to a certain proportion and stir evenly for 40 minutes. Then, defoaming the colloid (bubbles generated during the baking process are likely to cause light leakage from the chip). In the end, the colloid is spotted on the prepared blue chip and allowed to stand for 30 minutes, the device is baked in a drying oven at 150 °C for 1 hour, and the finished device is taken out after it is naturally cooled to room temperature.

2.3 Characterization

X-ray powder diffraction (XRD) was used to analyze the phase structure of the samples. The radiation source was Cu target Kα (λ = 0.15406 nm), the tube voltage was 40 kV, the tube current was 30 mA, the scanning speed was 5° min^{-1}, and the scanning range was 10–80°. Diffuse reflectance spectroscopy (DR): at room temperature (25 °C), the reflectance spectra of the sample was determined by Hitachi U-4100 diffuse reflectance spectrometer, with $BaSO_4$ as the background, and the wavelength scanning range was 200–800 nm. The emission spectra and excitation spectra of the sample were measured by Horiba FL-4600 fluorescence spectrometer. The detector model is iHR320, the excitation source is a xenon lamp of 450 W, the scanning speed is 1200 nm min^{-1}, the integration time is 0.1 s, and the width of the incident and exit slit is 2 nm.

3 Results and discussion

3.1 Phase formation and structure of CIG

Fig. S1† shows the crystal structure of $Ca_3In_2Ge_3O_{12}$ belongs to garnet structure, its space group is $Ia\bar{3}d$, and belongs to symmetrical cubic structure, lattice parameters $a = b = c =$ 12.58 (Å), $\alpha = \beta = \gamma = 90°$, $z = 8$. Ca^{2+} (r = 0.112 Å) ions occupy eight distorted dodecahedral sites coordinated by O^{2-} ions, and In^{3+} (r = 0.080 Å) and Ge^{4+} (r = 0.039 Å) ions occupy orthooctahedral sites and four O^{2-} coordinated tetrahedral sites respectively. In addition, in the chamfered view of the unit cell, each dodecahedron is connected to six octahedrons through a common edge, and each tetrahedron is connected to four octahedrons through a common vertex. The flexible structure provides a rich coordination environment for activators.

As shown in Fig. 1(a), the XRD patterns of CIG doped with different concentrations of Cr^{3+} corresponded to the positions of the main peak in the standard card one by one. A small amount of doping did not affect the crystal structure, and the synthesized samples were pure phase. The elemental mapping shows a uniform distribution of the Ca, In, Ge, O and Cr elements (Fig. 1(b)). Four samples with doping concentration x of 0.01, 0.03, 0.07 and 0.15 were refined by XRD using general

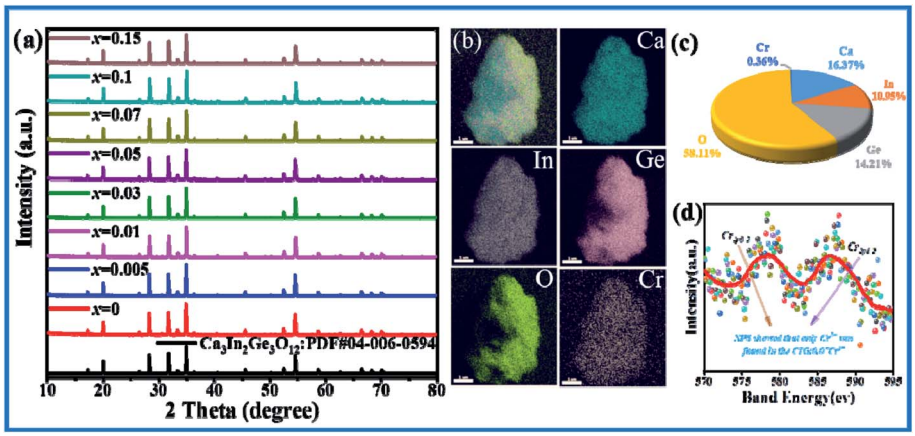

Fig. 1 (a) X-ray powder diffraction patterns of Cr^{3+} doped CIG. (b) Elemental mapping images of CIG:0.07Cr^{3+}. (c) Atomic % of CIG:0.07Cr^{3+}. (d) XPS spectrum of CIG:0.07Cr^{3+}.

structure analysis system (GSAS)[26] software. The results are shown in Table 1. It can be seen that with the increase of Cr^{3+} concentration, the cell volume V gradually decreases, which is due to substitution of In^{3+} by Cr^{3+} with smaller radius, indicating that Cr^{3+} has successfully entered the lattice structure and replaced In^{3+}. And the refined parameters $\chi^2 < 10$, $R_p < 10\%$ and $R_{wp} < 15\%$ are all within the error range. The calculated values in the refined Atlas (Fig. S2(a–d)†) are in good agreement with the measured values, which proves the rationality of the refined results. In addition, the EDX results of CIG:0.07Cr^{3+} show that the atomic ratio is close to the molecular formula (Fig. 1(c)), and the XPS spectrum shows that only $2p_{3/2}$ and $2p_{1/2}$ from Cr^{3+} can be detected (Fig. 1(d)). These results indicate that specific concentrations of Cr^{3+} were introduced into garnet homogeneously and the lattice structure was not destroyed.

3.2 Luminescence properties of CIG:xCr^{3+}

The excitation spectrum of CIG:0.07Cr^{3+} monitored at 804 nm and the emission spectrum at 480 nm are shown in Fig. 2(a). It can be seen that Cr^{3+} has three excitation bands of 230–350 nm, 350–550 nm and 550–750 nm in near UV to IR, which correspond to transitions of $^4A_2 \rightarrow {}^4T_1(^4p)$, $^4A_2 \rightarrow {}^4T_1(^4F)$, and $^4A_2 \rightarrow {}^4T_2(^4F)$, respectively. And CIG:0.07Cr^{3+} emits a wide spectrum near-infrared light of 650–1150 nm under excitation of 480 nm blue light. As shown in Fig. 2(b), with the increase of doping concentration, the emission intensity at the main peak position of phosphor first increases and then decreases, and the quenching point is at $x = 0.07$. It can be seen from the normalized emission spectra of the illustration that as the concentration of Cr^{3+} increases, the spectra are accompanied by a slight red shift. It may be caused by the change of crystal field. However, due to the small red shift amplitude, it is difficult to monitor and calculate the obvious change of the crystal field intensity. We can notice from Fig. 2(a) that there is a small overlap between the excitation and emission spectra, which may be one of the factors causing the red shift of the fluorescence. In addition, the diffuse reflectance spectra (DR) of the CIG:xCr^{3+} (x = 0.03, 0.05, 0.07, 0.15) are shown in Fig. 2(c). Three obvious reflection bands correspond to the three characteristic excitations of Cr^{3+}. According to the Kubelka–Munk equation, the band gap of the sample can be calculated:[27,28]

$$[F(R)h\nu]^2 = D(h\nu - E_g) \quad (1)$$

$$F(R) = (1 - R)^2/2R \quad (2)$$

where $h\nu$ represents photon energy, R represents reflection intensity, E_g represents optical band gap. As shown in the illustration, E_g can be represented by the tangent cross-section of the relationship curve between $[F(R)h\nu]^2$ and $h\nu$. As the doping concentration increases, the band gap of CIG gradually decreases. The distance between the ground state and the excited state gradually decreases, resulting in lower energy required for electronic transitions, and finally the spectra presents a red shift. In summary, the combined effect of

Table 1 Refined parameters of CIG:xCr^{3+} calculated by GSAS Refine Software

	CIG:0.005Cr^{3+}	CIG:0.03Cr^{3+}	CIG:0.07Cr^{3+}	CIG:0.15Cr^{3+}
Space group	$Ia\bar{3}d$	$Ia\bar{3}d$	$Ia\bar{3}d$	$Ia\bar{3}d$
Symmetry	Cubic	Cubic	Cubic	Cubic
$a/b/c$ (Å)	12.5841	12.5832	12.5796	12.5730
V (Å^3)	1992.877	1992.365	1990.661	1988.006
$\alpha/\beta/\gamma$ (deg)	90	90	90	90
R_p	8.49%	8.26%	8.61%	9.94%
R_{wp}	11.86%	11.18%	11.55%	12.99%

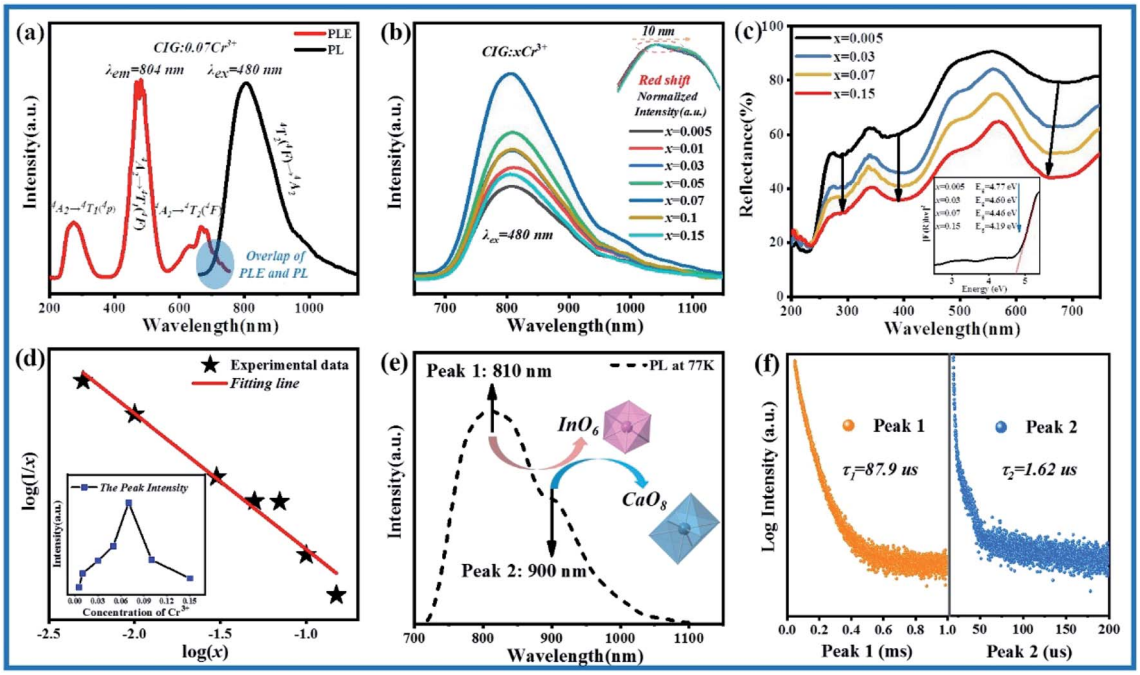

Fig. 2 (a) Excitation and emission spectra of CIG:0.07Cr^{3+}. (b) Emission spectra of CIG:xCr^{3+}. (c) Diffuse reflectance spectra (DR) of CIG:xCr^{3+}. (d) The liner relationship between log(I/x) and log(x). (e) Low-temperature spectrum at 77 K of CIG:0.07Cr^{3+}. (f) Lifetimes of peak 1 and peak 2.

radiation reabsorption and the reduction of the band gap leads to a red shift of the spectra. At the same time, radiation reabsorption is also one of the reasons for concentration quenching. Generally speaking, the main causes of concentration quenching are non-radiative energy transfer, including exchange interaction, radiation reabsorption and multipole interaction. The critical distance R_c between Cr^{3+} ions can be used as the judging mechanism. Only when it is less than 5 Å can exchange interaction occur. According to Blasse formula:[29]

$$R_c = 2\left[\frac{3V}{4\pi X_c N}\right]^{\frac{1}{3}} \quad (3)$$

where V represents the unit cell volume, X_c represents the critical concentration of Cr^{3+}, and N represents the number of cations in the cell. For CIG:0.07Cr^{3+}, $V = 1990.661$ Å^3, $X_c = 0.07$, $N = 8$, so the critical distance R_c of Cr^{3+} in this matrix is approximately equal to 7.63 Å > 5 Å, indicating that the main cause of quenching concentration is not exchange interaction. It can be seen from Fig. 2(a) that the excitation and emission spectra overlap slightly at 700–750 nm, which may cause radiation reabsorption and concentration quenching. In addition, there are interactions between multiple levels in the quenching mechanism of phosphor. According to Dexter theory, the ratio of emission intensity of phosphor to its corresponding concentration follows the following equation:[30–32]

$$I/x = k[1 + \beta(x)^{\theta/3}]^{-1} \quad (4)$$

In this formula, I represents the luminescence intensity, x is the activator concentration, k and β are constants for a given matrix under the same excitation. When θ is 6, 8, and 10, it represents dipole–dipole interaction, dipole–quadrupole interaction, and quadrupole–quadrupole interaction, respectively. If θ is 3, it represents the energy transfer between the nearest Cr^{3+} or the next closest Cr^{3+}. As shown in Fig. 2(d), in formula (4), the corresponding relationship between log(I/x) and log(x) can be synthesized into a straight line, with slope $K = -\theta/3 = -0.9035$, so $\theta = 2.7105$, which is the closest to 3. Therefore, the quenching mechanism of the phosphor is the radiation reabsorption phenomenon and the energy transfer between the closest or next closest Cr^{3+}.

In order to explore the luminescence mechanism of CIG:xCr^{3+}, the low-temperature spectrum of CIG:0.07Cr^{3+} was measured and given in Fig. 2(e). It can be seen that the emission spectrum measured at a temperature of 77 K shows peak 1 and peak 2 at 810 nm and 900 nm, representing two different emission centers exist. In order to prove the existence of the two peaks, the lifetimes of CIG:0.07Cr^{3+} were measured monitoring the emission at 810 nm and 900 nm respectively under the excitation of 480 nm, as shown in Fig. 2(f). The average life can be calculated by double exponential curve fitting:[33,34]

$$I = I_0 + A_1 \exp(-t/\tau_1) + A_2 \exp(-t/\tau_2) \quad (5)$$

$$\tau^* = (A_1\tau_1^2 + A_2\tau_2^2)/(A_1\tau_1 + A_2\tau_2) \quad (6)$$

Among them, τ_1 and τ_2 are fast and slow decay life, A_1 and A_2 are constants. After calculation, the lifetimes of peak 1 and peak

2 are 87.9 μs and 1.62 μs, respectively. The difference in magnitude indicates that they belong to two different luminescence centers. There are three potential luminescence centers in CIG: CaO_8, InO_6 and GeO_4. Cr^{3+} ions tend to emit in the weak crystal field, and are very unstable in the tetrahedral environment,[14] so it is speculated that one of the two luminescence centers comes from the octahedron InO_6 and the other from the dodecahedron CaO_8. And octahedral crystal field strength > dodecahedral crystal field strength,[35] strong crystal field corresponds to high emission energy, so peak 1 comes from octahedron, and peak 2 comes from dodecahedron. In addition, it is electronegative In (1.78) > Ca (1.00), so the covalence of InO_6 is less than CaO_8, and the nephelauxetic effect of InO_6 is less than CaO_8. In other words, the energy required to go from ground state to excited state: InO_6 > CaO_8, which also indicates that peak 1 is from octahedron, and peak 2 is from dodecahedron.

3.3 Luminescent properties of $CI_{2-x}G_xG$:0.07Cr^{3+}

The thermal stability of phosphor is an important index to measure phosphor. Generally the emission intensity of phosphor is affected by the heat generated during the process of diode emitting. Adjusting the structural rigidity of matrix through solid state method is an effective method to increase the temperature performance of phosphor. For the purpose of improving the thermal stability and emission intensity, cationic regulation was carried out based on the optimal doping concentration CIG:0.07Cr^{3+}. As is known to all, the 3d orbit of Cr^{3+} is exposed to the crystal field, so the luminescent properties of Cr^{3+} is greatly affected by the crystal field environment. Moreover, Ga^{3+} and In^{3+} belong to the same main group and can also exist in the matrix in the form of 6 coordination, so Ga^{3+} was introduced to adjust or improve the optical properties of phosphors. R (Ga^{3+}, $N = 6$) = 0.62 Å, R (In^{3+}, $N = 6$) = 0.8 Å, and R (Cr^{3+}, $N = 6$) = 0.615 Å. According to the doping formula, successful doping is considered when the radius difference between doped ions and substituted ions is less than 30%.[36,37]

$$D_r = \left| 100 \times \frac{R_m N - R_d(N)}{R_m(N)} \right| \quad (7)$$

where D_r represents the radius difference between the substituted ions and the doped ions, R_m and R_d represent the radii of the substituted ions and the doped ions respectively, and N represents the coordination number. According to the formula, D_r(In^{3+}–Cr^{3+}) = 23.125% and D_r (Ga^{3+}–Cr^{3+}) = 0.8%. Obviously, the matching degree of Cr^{3+} substituting for Ga^{3+} is better.

A series of $Ca_3In_{2-x}Ga_xGe_3O_{12}$ ($CI_{2-x}G_xG$):0.07Cr^{3+} phosphors are synthesized by using Ga^{3+} substituting for In^{3+} from part to the whole. As shown in Fig. 3(a), when the doping concentration of Ga^{3+} is 0%, the crystalline phase is in good agreement with PDF#04-006-0594. With the increase of Ga^{3+}, XRD clearly demonstrates the transition of the crystalline phase from $Ca_3In_2Ge_3O_{12}$:0.07Cr^{3+} to $Ca_3Ga_2Ge_3O_{12}$:0.07Cr^{3+}, and the peak position is shifted to a large angle, and finally matches well with PDF#00-011-0023. This phenomenon can be attributed to the lattice shrinkage caused by the substitution of small ions, as presented in Fig. 3(b). According to the Bragg equation:[38]

$$2d \sin\theta = k\lambda \quad (8)$$

where d is the spacing between crystals, θ represents the diffraction angle, k is the reflection level, and λ is the wavelength of X-ray. In this experiment, λ is a fixed value (Cu target K_α, λ = 0.15406 nm), so d is inversely proportional to θ. As the smaller Ga^{3+} gradually replaces the larger In^{3+}, the lattice shrinks, the spacing between the crystals decreases, and the diffraction angle increases, which also indicates the formation of a continuous solid solution. $Ca_3In_2Ge_3O_{12}$:0.07Cr^{3+} and $Ca_3Ga_2Ge_3O_{12}$:0.07Cr^{3+} both belong to the garnet structure with the same structure and the same spatial group, which is also the reason why their solid solubility is so great. As shown in Fig. 3(c), the SEM image shows that the phosphor is composed of smooth spheres of uneven size. In follow-up experiments some flux or dispersant can be added to control the morphology of the phosphor. In addition, EDX test was done on the sample of $CI_{0.2}G_{1.8}G$:0.07Cr^{3+}. The element content is listed in the inset table. The ratio of In to Ga is 1:9.3, which is very close to the molecular formula element ratio, which means the specific content Ga^{3+} replaced In^{3+} successfully.

All the $CI_{2-x}G_xG$:0.07Cr^{3+} (x = 0–2) samples emit broad spectra covering 650–1150 nm under the excitation of 480 nm, as shown in Fig. 4(a). With the concentration of Ga^{3+}(x) increases, the emission intensity increases significantly, and reaches the maximum value at $x = 1.8$, which is about 5 times the initial intensity. As shown in Fig. 4(b), the normalized emission spectra of $CI_{2-x}G_xG$:0.07Cr^{3+} show that the spectra have a blue shift of 50 nm, which is the result of the combined effect of the nephelauxetic effect and the changes of crystal field strength. The nephelauxetic effect is attributed to the change of the interaction between electrons, which causes the transition band between the electron energy levels to produce a slight shift. Due to the different covalent effects of different ligands, the effect on the spectra shows blue shift or red shift. It can be expressed by the following formula:[39]

$$1 - \beta = hk \quad (9)$$

where β represents the probability of electron cloud diffusion, h and k represent anionic ligand and metal respectively. The decrease in the repulsion between electrons or the increase in h parameter is due to the decrease in covalency, and the covalency of crystal material is related to the electronegativity of ions. The greater the covalency is, the more obvious the nephelauxetic effect is, and the greater the downward shift of the energy level is. The centroid shift can be calculated by the following formula:[40–42]

$$\varepsilon_c = \frac{e^2}{4\pi\varepsilon_0}\left(\langle r^2\rangle_{3d4s} - \langle r^2\rangle_{3d^5}\right)\sum_{i=1}^{N} \times \frac{{\alpha_{sp}}^i}{(R_i - 0.5\Delta R)^6} \quad (10)$$

$$A = \frac{e^2}{4\pi\varepsilon_0}\left(\langle r^2\rangle_{3d4s} - \langle r^2\rangle_{3d^5}\right) \quad (11)$$

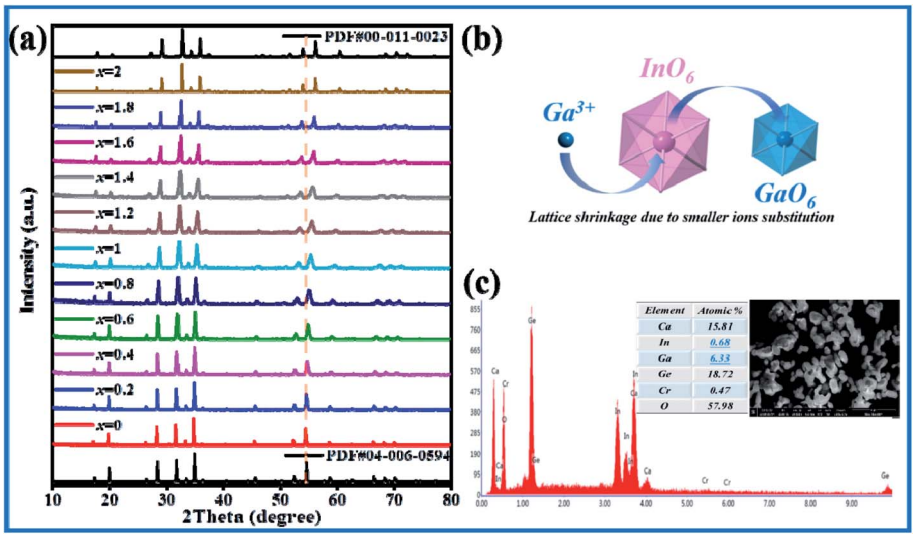

Fig. 3 (a) X-ray powder diffraction patterns of $Cl_{2-x}G_xG$:0.07Cr^{3+}. (b) Diagram of Ga^{3+} substituting for In^{3+}. (c) SEM and EDX diagrams of $Cl_{0.2}G_{1.8}G$:0.07Cr^{3+}.

$$\alpha_{sp}{}^{o} = 0.33 + 4.8/\chi_{av}{}^{2} \quad (12)$$

where r is the radial position on the 3d4s and $3d^5$ orbital, e is the elementary charge, R_i represents the distance between Cr^{3+} in the unit cell and the anion in the lattice, ΔR is the radius difference of Cr^{3+} (0.615 Å, $N = 6$) and In^{3+} (0.8 Å, $N = 6$). $0.5\Delta R$ is the correction of the lattice relaxation around the Cr^{3+} ion. N is the number of O^{2-} around Cr^{3+}. ε_0 is the dielectric constant of vacuum, A is a constant (10^{-20} m^2), $\alpha_{sp}{}^{o}$ represents O^{2-} spectral polarizability (10^{-30} m^3), the spectral polarizability is affected by the combined action of the ligand anion and the cation bound to the ligand anion, it is inversely proportional to the average electronegativity of the matrix cation $\chi_{av}{}^{2}$. The electronegativity of Ga^{3+} and In^{3+} is 1.81 and 1.78 respectively. As shown in Fig. 4(c), when more and more Ga^{3+} replaces In^{3+}, the average electronegativity of the unit cell will increase. A large proportion of substitution will make this effect more obvious.

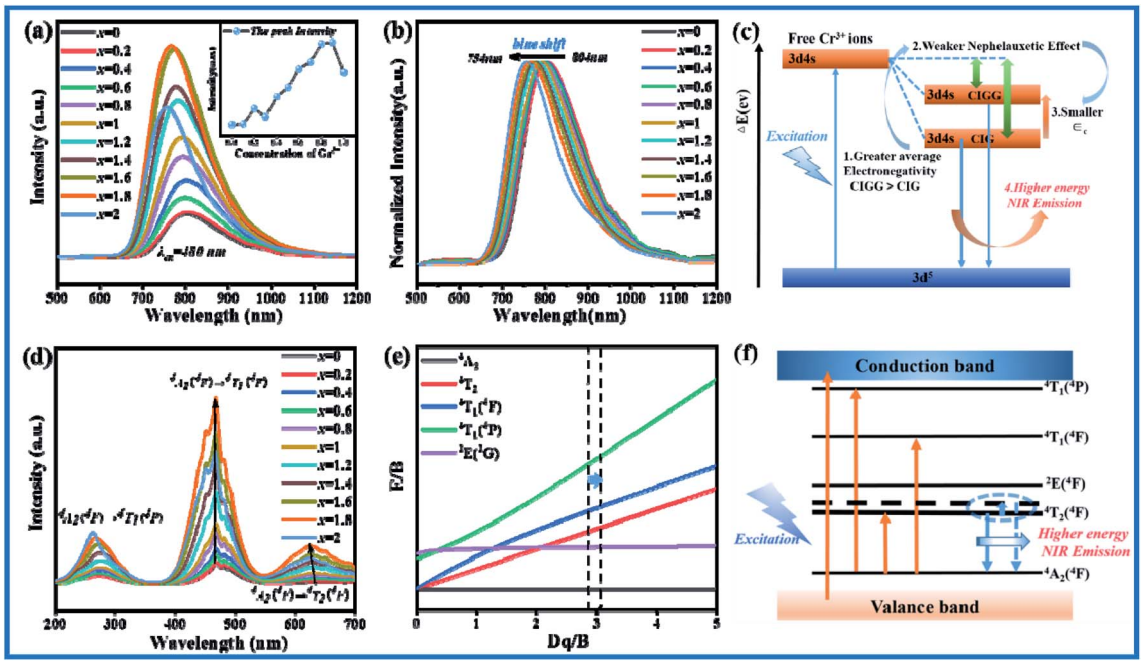

Fig. 4 (a) Emission spectra of $Cl_{2-x}G_xG$:0.07Cr^{3+} phosphors excited by 480 nm. (b) Normalized intensity emission spectra of $Cl_{2-x}G_xG$:0.07Cr^{3+}. (c) The influence of nephelauxetic effect on centroid shift. (d) Excitation spectra of different Ga^{3+} concentrations. (e) Tanabe–Sugano energy level diagram of $3d^3$ ions in an octahedral environment. (f) Energy level transition and $^4T_2$ energy levels shift diagram of Cr^{3+}.

As a result, the spectral polarizability of O^{2-} is reduced, and finally the center of mass displacement ε_c is reduced, the energy separation between the ground state and the excited state increases, and the energy required for electronic transition becomes higher, resulting in a blue shift of the emission spectra.

In addition to the nephelauxetic effect, the change of crystal field intensity is also an important cause of spectral shift. Fig. 4(d) is the excitation spectra of $CI_{2-x}G_xG{:}0.07Cr^{3+}$. The three excitation bands belong to the $^4A_2{}^4F \rightarrow {}^4T_1{}^4P$, $^4A_2{}^4F \rightarrow {}^4T_1{}^4F$, $^4A_2{}^4F \rightarrow {}^4T_2{}^4F$ transitions of Cr^{3+}. In the octahedron, it is mainly $^4A_2{}^4F \rightarrow {}^4T_1{}^4F$, $^4A_2{}^4F \rightarrow {}^4T_2{}^4F$. Among them, $^4A_2{}^4F \rightarrow {}^4T_2{}^4F$ is greatly affected by the most crystal field environment. With the increase of Ga^{3+}, the position of the peak of $^4A_2{}^4F \rightarrow {}^4T_1{}^4F$ is basically unchanged. The peak position of $^4A_2{}^4F \rightarrow {}^4T_2{}^4F$ is shifted to the left. According to the Tanabe–Sugano ($3d^3$) diagram (Fig. 4(e)), the relative positions of $^4T_1{}^4F$, $^4T_2{}^4F$ and $^2E(^2G)$ energy levels vary with the D_q/B value. According to the crystal field theory, the values of D_q/B can be determined by the following equations calculation:[43]

$$E(^4T_2) = 10D_q \tag{13}$$

$$\frac{D_q}{B} = \frac{15\left(\frac{\Delta E}{D_q} - 8\right)}{\left(\frac{\Delta E}{D_q}\right)^2 - 10\left(\frac{\Delta E}{D_q}\right)} \tag{14}$$

$$\Delta E = E(^4T_1) - E(^4T_2) \tag{15}$$

where D_q is the crystal field intensity, B is the Racha parameters, ΔE represents the energy difference between $^4T_1$ and $^4T_2$, and is determined by the peak positions of $^4T_1{}^4F$ and $^4T_2{}^4F$. The final results are shown in Table 2, as the doping concentration increases, D_q/B gradually increases. From Fig. 4(f), it can be seen that the energy difference between the energy level positions of $^4T_2{}^4F$ and $^4A_2{}^4F$ becomes larger, resulting in a blue shift of the spectra. In summary, the nephelauxetic effect and the crystal field effect work together to make the spectra blue shift.

In order to investigate whether the thermal stability of the material has been improved after doping Ga^{3+}, the temperature emission spectra of $CIG{:}0.07Cr^{3+}$ and $CI_{0.2}G_{1.8}G{:}0.07Cr^{3+}$ excited at 480 nm were measured and shown in Fig. 5(a). The emission intensity of both samples decreases when the temperature rises. The illustration shows $CI_{0.2}G_{1.8}G{:}0.07Cr^{3+}$ has better temperature stability than $CIG{:}0.07Cr^{3+}$. For phosphors, thermal quenching is caused by thermal ionization and thermal activation. Thermal ionization means that the electrons in the excited state are heated and reach the conduction band directly. The generation electron transfer does not return to the ground state by means of transition, so thermal quenching occurs. $CI_{0.2}G_{1.8}G{:}0.07Cr^{3+}$ phosphor has higher energy emission (Fig. 4(f)), so its $^4T_2$ energy level is closer to the conduction band, and the electrons on it are easier to be excited to the conduction band and form thermal quenching under the effect of thermal ionization. However, the thermal stability of $CI_{0.2}G_{1.8}G{:}0.07Cr^{3+}$ phosphor is greater than that of $CIG{:}0.07Cr^{3+}$ phosphor, so thermal ionization is not the main reason. On the other hand, thermal activation means that the electrons in the excited state level vibrate more and more during the heating process, cross the potential barrier and return to the ground state in the form of non radiative transition. Fig. 5(b) explains the reason for the different temperature quenching performance. With the increase of temperature, the energy of phonons increases, which leads to the decrease of transition probability and absorption intensity. The electrons in the excited state emit phonons, and the phonons relax to lower energy levels. When the Stokes shift $\Delta R_2 < \Delta R_1$, the energy required for phonon relaxation ΔE_2 is greater than ΔE_1. That is to say, the decrease of Stokes shift increases the energy required for phonon relaxation. Therefore, $CIG{:}0.07Cr^{3+}$ is greatly affected by temperature, and $CI_{0.2}G_{1.8}G{:}0.07Cr^{3+}$ is less affected by temperature. The Stokes shift is determined by the structural rigidity of the materials and the stronger the rigidity is, the smaller the stokes shift is.[44] We speculate that when smaller ions are introduced into the material, the more compact structure improves the rigidity of the material. George *et al.* used the Debye temperature ($\theta_{D,i}$) to represent the rigidity of the crystal lattice, and used the high temperature approximation method to compare the Debye temperature of different atoms in crystallography according to isotropic atomic displacement parameters:[45,46]

$$\theta_{D,i} = \sqrt{\frac{3h^2TN_A}{A_i k_B U_{iso,i}}} \tag{16}$$

The Debye temperature is inversely proportional to the atomic displacement parameter U_{iso}. According to the refined data, the corresponding atomic displacement parameters U_{iso} of Ca, In, Ge in $CIG{:}0.07Cr^{3+}$ are 0.04992, 0.05047, 0.05473, the average is 0.05171. In $CI_{0.2}G_{1.8}G{:}0.07Cr^{3+}$, the corresponding atomic displacement parameters of Ca, In, and Ge are 0.00348, 0.00114, 0.00293, and the average is 0.00252. Obviously, the average atomic displacement parameter of $CI_{0.2}G_{1.8}G{:}0.07Cr^{3+}$ is smaller than $CIG{:}0.07Cr^{3+}$, so its corresponding higher Debye temperature and higher structure rigidity. This is consistent with our conjecture. Therefore, the better thermal quenching performance of $CI_{0.2}G_{1.8}G{:}0.07Cr^{3+}$ is attributed to the better structural rigidity.

Table 2 Results of D_q/B of $Ca_3In_{2-x}Ga_xGe_3O_{12}{:}0.07Cr^{3+}$ ($x = 0.2$–2)

x	$^4A_2$–$^4T_2(^4F)$ λ(nm)	$^4A_2$–$^4T_1(^4F)$ λ(nm)	D_q/B
0.2	637	467	2.8248
0.4	636	467	2.8458
0.6	632	467	2.9325
0.8	631	467	2.9547
1	630	467	2.9772
1.2	628	467	3.0229
1.4	627	467	3.0461
1.6	626	467	3.0697
1.8	625	467	3.0934
2	623	467	3.1418

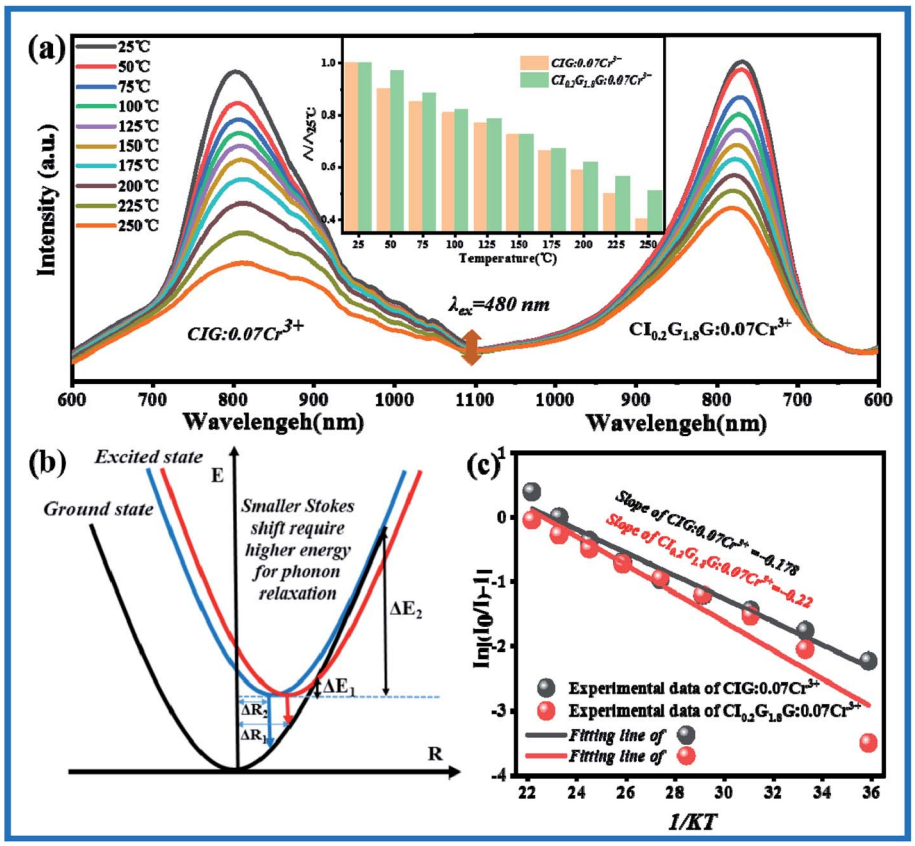

Fig. 5 (a) The temperature emission spectra of CIG:0.07Cr^{3+} and $CI_{0.2}G_{1.8}G$:0.07Cr^{3+} excited by 480 nm. (b) Configuration coordinate of Stokes shift affecting phonon relaxation. (c) Fitting curves of variable temperature activation energy for CIG:0.07Cr^{3+} and $CI_{0.2}G_{1.8}G$:0.07Cr^{3+}.

To further understand the thermal quenching phenomenon, we use the Arrhenius formula to express $\ln[(I_0/I) - 1]$ and $1/KT$ to calculate the thermal quenching activation energy of the sample:[47]

$$I_T = \frac{I_0}{I + c\exp\left(-\frac{\Delta E}{KT}\right)} \quad (17)$$

among them, I_T represents the emission intensity at different temperatures, I_0 represents the emission intensity of the sample at 25 °C, ΔE is the thermal quenching activation energy, and K is the Boltzmann constant (8.626×10^{-5} eV). Through the above formula, the relationship between $\ln[(I_0/I) - 1]$ and $1/KT$ can be expressed as a straight line, the absolute value of the slope of the straight line is the thermal quenching activation energy ΔE, as shown in Fig. 5(c), CIG:0.07Cr^{3+} thermal quenching activation energy is 0.178. The thermal quenching activation energy of $CI_{0.2}G_{1.8}G$:0.07Cr^{3+} is 0.22, which increased by 24%, reaching a relatively reliable value. And We have summarized the Cr^{3+} near-infrared luminescent phosphors reported in the last year or two, and intuitively compared the ratio of the emission spectrum intensity (peak intensity) of these fluorescent materials at high temperature to normal temperature. It can be seen from Table 3 that $Ca_3In_{0.2}Ga_{1.8}Ge_3O_{12}$:$Cr^{3+}$ phosphor has relatively good temperature stability, which is very important for the application of pc-LED.

4 Application

As shown in Fig. 6(a), the cost of the phosphor adjusted by Ga^{3+} is not only greatly reduced to 30% of the original cost, but also the emission intensity is increased by more than five times, and the thermal quenching activation energy is also increased by 24%. These advantages make it extremely potential for commercial pc-LED applications. The DR of $CI_{0.2}G_{1.8}G$:0.07Cr^{3+} phosphor was shown in Fig. S3† and the strong absorption near 450 nm reveals the remarkable potential for the combination with the blue LED chip. We mixed $CI_{0.2}G_{1.8}G$:0.07Cr^{3+} with silica gel uniformly, and then package the blue chip together into pc-LED and its emission spectra under various drive currents were shown in Fig. S4,† which proves the stability and brightness adjustability of the LED chip. The emission spectra of the pc-LED and its potential applications are given in Fig. 6(b), the absorption light of 715–1050 nm overlaps with chlorophyll of photosynthetic bacteria and 700–800 nm overlaps with phytochrome (Pfr), so that it can be applied to far-red light plant illumination. Moreover, the emission band includes absorption peaks such as human oxyhemoglobin (890 nm) and cytochrome oxidase (820–840 nm), so it also has potential in human detection. Finally, the penetration depth of the photon in the silicon material increases exponentially with the increase of the wavelength. The penetration depth of the photon with the wavelength of 460 nm is only 0.28 μm, while the penetration

Table 3 Temperature stability of different Cr^{3+} doped phosphors

Samples	λ_{em} (nm)	$\Delta_{150°C}/\Delta$	$\Delta_{200°C}/\Delta$	$\Delta_{250°C}/\Delta$	ΔE (eV)	Ref.
$La_3Ga_5GeO_{14}:Cr^{3+}$	750–1400	20%	10%	—	0.297	48
$Ca_3Sc_2Si_3O_{12}:Cr^{3+}$	700–900	54%	32%	~10%	—	49
$La_2MgZrO_6:Cr^{3+}$	600–1200	~42%	—	—	0.089	50
$Y_2CaAl_4SiO_{12}:Cr^{3+}$	600–1100	78%	~68%	—	0.206	51
$ScBO_3:Cr^{3+}$	650–1000	51%	~30%	~19%	0.36	52
$Ca_2LuScGa_2Ge_2O_{12}:Cr^{3+}$	650–1100	57%	40%	—	0.17/0.49	53
$Ca_3In_{0.2}Ga_{1.8}Ge_3O_{12}:Cr^{3+}$	650–1150	73%	62%	51%	0.22	This work

depth of the photon with the wavelength of 750 nm is greater than 10 μm, indicating that such phosphor powder has great application potential in the silica-based solar spectra conversion technology. The experiment of far-infrared light plant illumination was designed: two branches of *Scindapsus aureus* with similar size were used for hydroponic culture in the same sunlight. One of them was irradiated with pc-LED of $CI_{0.2}G_{1.8}G:0.07Cr^{3+}$, and the other was not irradiated as control group, as depicted in Fig. 6(c). It can be observed that the experimental group grew longer roots after three weeks, and the secondary rooting appeared, which suggested that the stage of root differentiation was higher in the experimental group. Pfr absorbed 700–800 nm near-infrared light and promoted the transition to Pr, which promoted the growth of roots, indicating the application potential of $CI_{0.2}G_{1.8}G:0.07Cr^{3+}$ in the near-infrared plant lighting field.

5 Conclusions

In summary, a series of novel NIR phosphors with broad emission band (650–1150 nm) were synthesized by high temperature solid state method. $Ca_3In_{2-x}Ge_3O_{12}:xCr^{3+}$ has a garnet structure providing an abundant coordination environment for Cr^{3+} to produce NIR emission. The existence of two luminescence centers has been demonstrated by testing low-temperature spectra and decay curves. In addition, in order to improve the properties of $Ca_3In_{2-x}Ge_3O_{12}:xCr^{3+}$, a series of

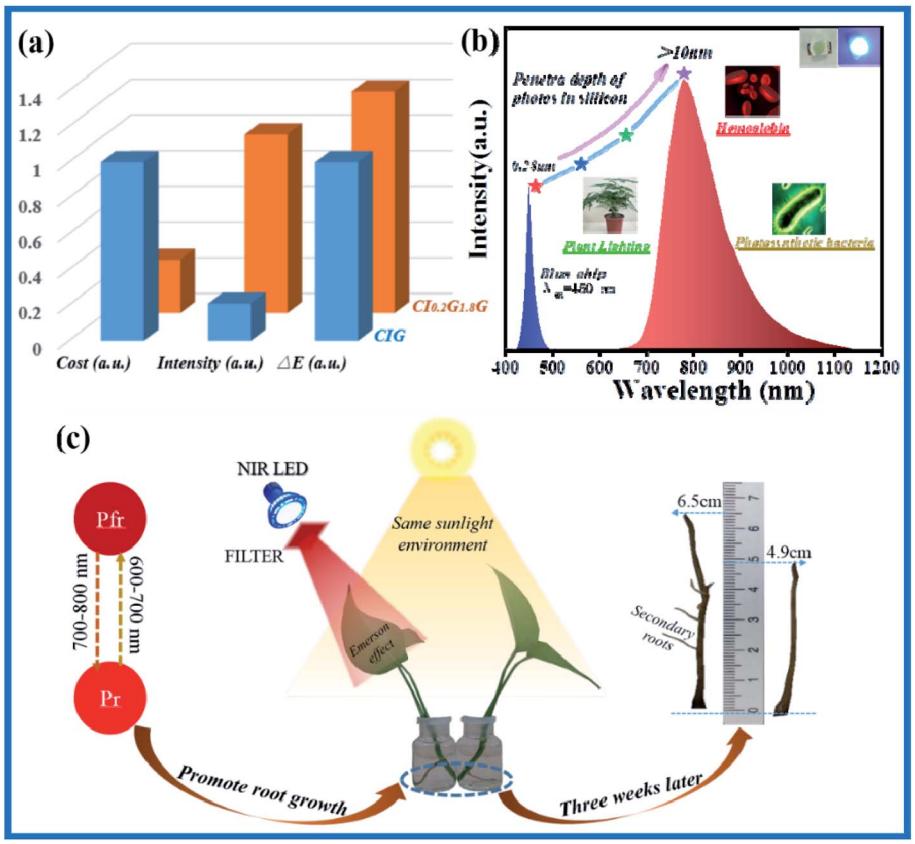

Fig. 6 (a) The comparison of cost, emission intensity, and thermal stability of phosphors before and after doping Ga^{3+}. (b)The emission spectra of pc-LED with $CI_{0.2}G_{1.8}G:0.07Cr^{3+}$ exited by 450 nm blue chip and its application potential. (c) Schematic diagram of near-infrared light plant illumination promoting root growth.

$Ca_3In_{2-x}Ga_xGe_3O_{12}$:0.07$Cr^{3+}$ were obtained by Ga^{3+} substituting for In^{3+}, which enhanced the emission intensity and led to blue shift of spectra through weakening the diffusion effect of the nephelauxetic effect and enhancing the crystal field strength. At the same time, the structural rigidity was represented by Debye temperature to explain the improvement of thermal stability. Finally, the application potential of this material is demonstrated by an experiment in the near-infrared plant illumination filed.

Conflicts of interest

The authors declare no competing financial interest.

Acknowledgements

The work is supported by the National Natural Science Foundation of China (No.51672066, 51902080, 12004093), the Funds for Distinguished Young Scientists of Hebei Province, China (No. A2018201101), and the Natural Science Foundation of Hebei Province, China (No. E2019201223), the personnel training project of Hebei Province, China (No. A201902005).

References

1 J. C. Ye, S. Tak, K. E. Jang, *et al.*, Nirs-spm: statistical parametric mapping for near-infrared spectroscopy, *Neuroimage*, 2009, **44**(2), 428–447.
2 B. Zeng, Z. Huang, A. Singh, Y. Yao, A. K. Azad, A. D. Mohite, *et al.*, Hybrid graphene metasurfaces for high-speed mid-infrared light modulation and single-pixel imaging, *Light: Sci. Appl.*, 2018, **7**(005), 523–530.
3 R. Weissleder and M. J. Pittet, Imaging in the era of molecular oncology, *Nature*, 2008, **452**(7187), 580–589.
4 F. F. Jobsis-vander Vliet, Discovery of the near-infrared window into the body and the early development of near-infrared spectroscopy, *J. Biomed. Opt.*, 1999, **4**(4), 392–396.
5 R. C. Morrow, Led lighting in Horticulture, *Hortence*, 2008, **43**(7), 1947–1950.
6 M. Cioc, A. Szewczyk, M. Zupnik, A. Kalisz and B. E. Pawlowska. Led lighting affects plant growth, morphogenesis and phytochemical contents of myrtus communis L. *in vitro*. *Plant Cell Tissue & Organ Culture*. 2017.
7 K. Okamoto, T. Yanagi, S. Takita, M. Tanaka and H. Watanabe, Development of plant growth apparatus using blue and red led as artificial light source, *Acta Hortic*, 1996, **440**(440), 111–116.
8 L. Wang, D. W. Sun, H. Pu and J. H. Cheng, Quality analysis and classification and authentication of liquid foods by near-infrared spectroscopy: a review of recent research developments, *Crit. Rev. Food Technol.*, 2016, **57**(7), 1524–1538.
9 A. Guelpa, F. Marini, A. Du Plessis, R. Slabbert and M. Manley, Verification of authenticity of south african honey and fraud detection using NIR spectroscopy, *Food Control*, 2016, DOI: 10.1016/j.foodcont.2016.11.002.
10 C. Wang, X. Wang, Y. Zhou, S. Zhang and H. Jiao, An Ultra-Broadband Near-infrared Cr^{3+}-activated Gallogermanate $Mg_3Ga_2GeO_8$ phosphor as Light sources for food analysis, *ACS Appl. Electron. Mater.*, 2019, **1**, 1046–1053.
11 L. Zhang, D. Wang, Z. Hao, X. Zhang, G. H. Pan, H. Wu, *et al.*, Cr^{3+}-doped broadband NIR Garnet Phosphor with Enhanced Luminescence and its Application in NIR spectroscopy, *Adv. Opt. Mater.*, 2019, **7**(12), 1900185.1–1900185.8.
12 Z. Pan, Y. Y. Lu and F. Liu, Sunlight-activated long-persistent luminescence in the near-infrared from Cr^{3+}-doped zinc gallogermanates, *Nat. Mater.*, 2012, **11**(1), 58–63.
13 S. Liu, Z. Wang, H. Cai, Z. Song and Q. L. Liu, Highly efficient near-infrared phosphor $LaMgGa_{11}O_{19}$:Cr^{3+}, *Inorg. Chem. Front.*, 2020, **7**, DOI: 10.1039/D0QI00063A.
14 G. Liu, M. S. Molokeev and B. Lei, Two-site Cr^{3+} occupation in the $MgTa_2O_6$:Cr^{3+} phosphor toward broad-band near-infrared emission for vessel visualization, *J. Mater. Chem. C*, 2020, **8**, DOI: 10.1039/D0TC01951H.
15 J. Qiao, G. Zhou and Y. Zhou, Divalent europium-doped near-infrared-emitting phosphor for light-emitting diodes, *Nat. Commun.*, 2019, **10**(1), DOI: 10.1038/s41467-019-13293-0.
16 A. Kux, S. Bertram, F. T. Hufert, H. Schmitz and W. Strek, Site selection spectroscopy of Cr^{3+} in $MgAl_2O_4$ green spinel, *J. Lumin.*, 1996, **68**(2), 91–103.
17 Y. J. Chuang, Photostimulated Near-Infrared persistent luminescence as a new optical read-out from Cr^{3+}-doped $LiGa_5O_8$, *Sci. Rep.*, 2013, **3**(3), 1554.
18 Y. Li, Y. Li, R. Chen, K. Sharafudeen, S. Zhou, M. Gecevicius, *et al.*, Tailoring of the trap distribution and crystal field in Cr^{3+}-doped non-gallate phosphors with near-infrared long-persistence phosphorescence, *NPG Asia Mater.*, 2015, **7**(5), e180.
19 Z. Akvil, B. Skirmante, Z. Arturas, V. Pranciskus and K. Aivaras, Sol-gel synthesized far-red chromium-doped garnet phosphors for phosphor-conversion light-emitting diodes that meet the photomorphogenetic needs of plants, *Appl. Opt.*, 2014, **53**(5), 907–914.
20 L. Zhang, S. Zhang, Z. Hao, X. Zhang, G. H. Pan, Y. Luo, *et al.*, A high efficiency Broad-Band Near-Infrared $Ca_2LuZr_2Al_3O_{12}$:Cr^{3+} Garnet Phosphor for blue led chips, *J. Mater. Chem. C*, 2018, **6**(18), 4967–4976.
21 M. Beata, M. Andries and J. Thomas, Temperature dependent Cr^{3+} photoluminescence in Garnets of the Type $X_3Sc_2Ga_3O_{12}$ (x = Lu, Y, Gd, La), *J. Lumin.*, 2018, DOI: 10.1016/j.jlumin.2018.05.076.
22 H. Lin, J. Xu, Q. M. Huang, B. Wang, *et al.*, Bandgap tailoring *via* si doping in inverse-garnet $Mg_3Y_2Ge_3O_{12}$:Ce^{3+} persistent phosphor potentially applicable in ac-led, *ACS Appl. Mater. Interfaces*, 2015, **7**(39), 21835.
23 H. Lin, B. Wang, Q. Huang, F. Huang, J. Xu and H. Chen, $Lu_2CaMg_2(Si_{1-x}Ge_x)_3O_{12}$:$Ce^{3+}$ solid-solution phosphors: Bandgap Engineering for Blue-Light activated Afterglow Applicable to ac-led, *J. Mater. Chem. C*, 2016, **4**(43), DOI: 10.1039/C6TC03818B.
24 J. K. Han, M. E. Hannah, A. Piquette, J. B. Talbot, K. C. Mishra and J. Mckittrick, Europium-Activated

KSrpo4- (Ba, Sr)$_2$SiO$_4$ solid solutions as color-tunable phosphors for Near-UV Light-Emitting diode applications, *J. Am. Ceram. Soc.*, 2013, **96**(5), 1526–1532.

25 Z. Xia, Z. Xu, M. Chen and Q. L. Liu, Recent developments in the new inorganic solid-state led phosphors, *Dalton Trans.*, 2016, 11214.

26 B. H. Toby, EXPGUI, a graphical user interface for GSAS, *J. Appl. Crystallogr.*, 2001, **34**(34), 210–213.

27 X. Chen, Z. Xia and Q. Liu, Synthesis, structure and luminescence properties of new chloro-germanate phosphors $Ca_3GeO_4Cl_2$:Eu^{2+}, *Dalton Trans.*, 2014, **43**, 13370.

28 C.-H. Huang and T.-M. Chen, Novel yellow-emitting $Sr_8MgLn(PO_4)_7$:Eu^{2+} (Ln=Y, La) phosphors for applications in White LEDs with excellent color rendering index, *Cheminform*, 2011, **42**(35), 5725–5730.

29 G. Blasse, Energy transfer between inequivalent Eu^{2+} ions, *J. Solid State Chem.*, 1986, **62**(2), 207–211.

30 W. Z. Sun, Y. L. Jia, P. Pang, H. F. Li, T. F. Ma, D. Li, *et al.*, $Sr_9Mg_{1.5}(PO_4)_7$:Eu^{2+}: a novel broadband orange-yellow-emitting phosphor for blue light-excited warm white leds, *ACS Appl. Mater. Interfaces*, 2015, **7**(45), 25219–25226.

31 T. Gao, W. Zhuang, R. Liu, Y. Liu and X. Chen, Design of a broadband NIR phosphor for Security-Monitoring LEDs: Tunable Photoluminescence Properties and Enhanced Thermal Stability, *Cryst. Growth Des.*, 2020, DOI: 10.1021/acs.cgd.0c00154.

32 V. L. G. Uitert, Characterization of energy transfer interactions between rare earth ions, *J. Electrochem. Soc.*, 1967, **114**(10), 1048.

33 K. Li, M. J. Xu, X. Cai, J. Fan, Y. Zhang, M. Shang, *et al.*, An efficient green-emitting α-$Ca_{1.65}Sr_{0.35}SiO_4$:Eu^{2+} phosphor for Uv/n-Uv w-LEDs: synthesis, luminescence and thermal properties, *J. Mater. Chem. C*, 2015, **3**, 1–9.

34 K. Li, M. Xu, J. Fan, M. Shang, H. Lian and J. Lin, Tunable green to yellowish-orange phosphor $Na_3LuSi_2O_7$:Eu^{2+}, Mn^{2+} *via* energy transfer for UV-LEDs, *J. Mater. Chem. C*, 2015, 1–9.

35 H. H. Lin, G. G. Bai, T. Yu, *et al.*, Site Occupancy and Near-Infrared Luminescence in $Ca_3Ga_2Ge_3O_{12}$: Cr^{3+} Persistent Phosphor, *Adv. Opt. Mater.*, 2017, 1077227.

36 A. M. Pires and M. R. Davolos, Luminescence of Europium(iii) and Manganese(ii) in Barium and Zinc orthosilicate, *Chem. Mater.*, 2001, **13**(1), 21–27.

37 M. Y. Peng, Z. W. Pei, G. Y. Hong and Q. Su, The reduction of Eu^{3+} to Eu^{2+} in $BaMgSiO_4$: Eu prepared in air and the luminescence of $BaMgSiO_4$:Eu^{2+} phosphor, *J. Mater. Chem.*, 2003, **13**, 1202–1205.

38 J. Kacher, C. Landon, B. L. Adams and D. Fullwood, Bragg's law diffraction simulations for electron backscatter diffraction analysis, *Ultramicroscopy*, 2009, **109**(9), 1148–1156.

39 G. Li, Y. Tian, Y. Zhao and J. Lin, Recent progress in luminescence tuning of Ce^{3+} and Eu^{2+}-activated phosphors for pc-WLEDs, *Chem. Soc. Rev.*, 2015, **44**(23), 688–713.

40 P. Dorenbos, Calculation of the energy of the 5d barycenter of $La_3F_3[Si_3O_9]$: Ce^{3+}, *J. Lumin.*, 2003, **105**(2), 117–119.

41 P. Dorenbos, 5d-level energies of Ce^{3+} Fluoride I. and the crystalline environment. compounds, *Phys. Rev. B*, 2000, **62**(23), 15640–15649.

42 Q. Bai, S. Zhao, L. Guan, Z. J. Wang, P. L. Li and Z. Xu, Design and control of the luminescence of Cr^{3+}-doped phosphors in the near-infrared I region by fitting the crystal field, *Cryst. Growth Des.*, 2018, **18**, 3178–3186.

43 L. Li, Y. Yu, Z. L. Wang and Z. Lin, Crystal growth, spectral properties and crystal field analysis of Cr^{3+}: $MgWo_4$, *Crystengcomm*, 2013, **15**, 6089.

44 G. Blasse, B. C. Grabmaier *Luminescent Materials*. Springer-Verlag: Berlin, 1994.

45 N. C. George, A. J. Pell, G. Dantelle, K. Page and M. Anna Llobet, Balasubramania. Local environments of dilute activator ions in the solid-state lighting phosphor $Y_{3-x}Ce_xAl_5O_{12}$, *Chem. Mater.*, 2013, **25**, 3979–3995.

46 N. C. George, A. Birkel and J. Brgoch, Average and local structural origins of the optical properties of the nitride phosphor $La_{(3-x)}Ce_{(x)}Si_6N_{11}$ ($0 < x \leq 3$), *Inorg. Chem.*, 2013, **52**(23), DOI: 10.1021/ic402318k.

47 J. Laidler Keith, The development of the arrhenius equation, *J. Chem. Educ.*, 1984, **61**(6), 494.

48 T. Gao, W. Zhuang and R. Liu, Site occupancy and enhanced luminescence of broadband NIR gallogermanate phosphors by energy transfer, *J. Am. Ceram. Soc.*, 2020, **103**(1), DOI: 10.1111/jace.16685.

49 Z. Jia, C. Yuan and R. Li, Electron–phonon coupling mechanisms of broadband near-infrared emissions from Cr^{3+} in the $Ca_3Sc_2Si_3O_{12}$ garnet, *Phys. Chem. Chem. Phys.*, 2020, **22**, DOI: 10.1039/D0CP00240B.

50 H. Zeng, T. Zhou and L. Wang, Two-Site Occupation for Exploring Ultra-Broadband Near-Infrared Phosphor—Double-Perovskite La_2MgZrO_6:Cr^{3+}, *Chem. Mater.*, 2019, **31**(14), DOI: 10.1021/acs.chemmater.9b01587.

51 M. Mao, T. Zhou and H. Zeng, Broadband near-infrared (NIR) emission realized by the crystal-field engineering of $Y_{3-x}Ca_xAl_{5-x}Si_xO_{12}$:$Cr^{3+}$ (x=0-2.0) garnet phosphors, *J. Mater. Chem. C*, 2020, **8**, 1981–1988.

52 Q. Shao, H. Ding and L. Yao, Photoluminescence properties of a $ScBO_3$:Cr^{3+} phosphor and its applications for broadband near-infrared LEDs, *RSC Adv.*, 2018, **8**, 12035–12042.

53 B. Bai, P. Dang and D. Huang, Broadband Near-Infrared Emitting $Ca_2LuScGa_2Ge_2O_{12}$:Cr^{3+} Phosphors: Luminescence Properties and Application in Light-Emitting Diodes, *Inorg. Chem.*, 2020, **59**(18), DOI: 10.1021/acs.inorgchem.0c01890.